Nuclear Science and Techniques (2025) 36:73
https://doi.org/10.1007/s41365-025-01667-7

Detector array with digital data acquisition system for charged-particle decay studies

Hao Jian[1,2] · Xin-Xing Xu[1,2,3] · Kai-Long Wang[1,2] · Jia-Jian Liu[1,2] · Chao-Yi Fu[4] · Peng-Jie Li[1] · Yan-Yun Yang[1,2] · Guang-Xin Zhang[5] · Kang Wang[1,2] · Fang-Fang Duan[1,2] · Long-Hui Ru[1,2] · Guang-Shun Li[1,2] · Bing Ding[1,2] · Yun-Hua Qiang[1,2] · Cen-Xi Yuan[5] · Jun-Bing Ma[1,2] · Shi-Wei Xu[1,2] · Yu-Feng Gao[1,2] · Rui Fan[1,2] · Fan-Chao Dai[1,2] · Si-Xian Zha[4] · Hao-Fan Zhu[1,2] · Jin-Hai Li[1,2] · Shu-Lian Qin[1,2] · Zhi-Fang Chang[1,2] · Cheng Kong[1,2] · He-Xuan Yan[1,2] · Hao-Wei Xu[1,2] · Jia-Long Ning[1,2] · Bo-Ren Liu[1,2] · Jie Zhou[1,2] · Yu-Dong Chen[1,2] · Bo-Shuai Cai[5] · Yu-Ting Wang[6] · Hong-Yi Wu[7,8] · Zhi-Xuan Wang[5] · Dong-Sheng Hou[1,4] · Hu-Shan Xu[1,2,3] · Xiao-Hong Zhou[1,2,3] · Yu-Hu Zhang[1,2,3] · Meng Wang[1,2,3] · Zheng-Guo Hu[1,2,3] · Jenny Lee[4]

Received: 23 August 2024 / Revised: 18 November 2024 / Accepted: 20 December 2024 / Published online: 12 March 2025

Abstract
A state-of-the-art detector array with a digital data acquisition system has been developed for charged-particle decay studies, including β-delayed protons, α decay, and direct proton emissions from exotic proton-rich nuclei. The digital data acquisition system enables precise synchronization and processing of complex signals from various detectors, such as plastic scintillators, silicon detectors, and germanium γ detectors. The system's performance was evaluated using the β decay of ^{32}Ar and its neighboring nuclei, produced via projectile fragmentation at the first Radioactive Ion Beam Line in Lanzhou (RIBLL1). Key measurements, including the half-life, charged-particle spectrum, and γ-ray spectrum, were obtained and compared with previous results for validation. Using the implantation–decay method, the isotopes of interest were implanted into two double-sided silicon strip detectors, where their subsequent decays were measured and correlated with preceding implantations using both position and time information. This detection system has potential for further applications, including the study of β-delayed charged-particle decay and direct proton emissions from even more exotic proton-rich nuclei.

Keywords β-delayed proton decay · Double-sided silicon strip detector · High-purity germanium detector · Digital data acquisition system · Implantation–decay correlation

1 Introduction

Proton-rich nuclei far from stability exhibit a range of unique decay processes, particularly β-delayed charged-particle emissions and direct particle emissions. Spectroscopic studies of β-delayed proton decay and direct proton radioactivity have proven to be powerful tools for investigating the intricate properties of exotic nuclei near and beyond the proton drip line. The resonant proton capture reaction rates of the continuum states in weakly bound nuclei, which play a crucial role in astrophysical processes, can be determined by studying the properties of nuclear states near the proton separation threshold [1–3]. To observe decays from these states, as well as direct proton emissions from the ground state, it is essential to employ a detection system with a low energy threshold and high detection efficiency.

This work was supported by the National Key Research and Development Project, China (No.2023YFA1606404), the Strategic Priority Research Program of Chinese Academy of Sciences (No. XDB34010300), the National Natural Science Foundation of China (Nos. 12022501, 12105329, 12475127), the Guangdong Major Project of Basic and Applied Basic Research (No. 2021B0301030006), the Research Program of Heavy Ion Science and Technology Key Laboratory, Institute of Modern Physics, Chinese Academy of Sciences (Nos. HIST2024KS04, HIST2024CO04), Longyuan Youth Innovation and Entrepreneurship Talent Project of Gansu Province (No. 2024GZT04), State Key Laboratory of Nuclear Physics and Technology, Peking University (No. NPT2023KFY01), and the Major Science and Technology Projects in Gansu Province (No. 24GD13GA005).

Extended author information available on the last page of the article

The investigation of β-delayed charged-particle decay in proton-rich nuclei is typically conducted using two principal detection methods: the implantation–decay method with a silicon detector array [1–3] and the time-projection chamber (TPC) detection method [4–8]. The fundamental principles of the implantation–decay method are as follows: The nuclei of interest are implanted and stopped within a detector array. The decay energies of the β-delayed charged particles can then be measured with high accuracy, as the decay occurs directly within the implantation detector.

The correlation between implantation and decay events provides a unique opportunity to derive decay time and decay energy spectra, enabling detailed characterization of the decay properties exhibited by radioactive species. To ensure accurate measurements, the effects of dead layers in silicon detectors must be taken into account when β-delayed charged particles are stopped inside the silicon detector. This capability has driven the development of double-sided silicon strip detectors (DSSDs), which have become cutting-edge instruments for investigating these intriguing decay modes. Additionally, a germanium double-sided strip detector [9] can also serve as an implantation detector in certain experimental setups. A wide range of experiments in β-decay spectroscopy and proton radioactivity have significantly advanced our understanding of exotic nuclei properties. Notable examples include studies on ^{54}Zn [10], ^{45}Fe [11, 12], ^{27}S [13, 14], ^{26}P [15–17], ^{22}Si [18, 19], ^{22}Al [20–22], and ^{21}Mg [23]. Compared to silicon detectors, time-projection chamber (TPC) measurements offer direct and comprehensive insights into decay processes. For example, TPCs have facilitated studies of two-proton emissions from ^{45}Fe [4] and ^{54}Zn [5], as well as β-decay spectroscopy [6, 7]. The TPC detection method can facilitate the establishment of angular and momentum correlations between particles in multiparticle emissions [8]. In contrast, the DSSD-based implantation–decay method provides the precision required for high-resolution spectroscopy measurements [18, 19, 24].

Conventional analog data acquisition systems have been widely employed using various standards, such as Computer-Automated Measurement and Control (CAMAC) and the Versa Module Eurocard (VME) [25–27]. An analog system typically comprises preamplifiers, shaping amplifiers, and analog-to-digital converters (ADCs) for the analog signal channel, and fast amplifiers, discriminators, and time-to-digital converters (TDCs) for timing signals. Trigger signals are generally generated by the coincidence of selected fast signals corresponding to the physical process of interest. In recent years, digital data acquisition systems (DDAQs) have become increasingly prevalent in nuclear physics experiments [28–30], driven by advancements in fast digitizing technologies. In a DDAQ system, signals from preamplifiers are directly sampled and digitized, requiring high sampling frequencies (typically exceeding 100 MHz) and high-resolution sampling (12, 14, or 16 bits) to preserve the original analog signal information [31–34]. Subsequently, energy and timing information from detector outputs can be extracted using advanced numerical algorithms applied to the recorded signal waveforms. The flexibility provided by the wide range of pulse-shape analysis methods is essential for addressing the diverse demands of nuclear physics experiments. This approach offers significant advantages over traditional analog electronics, driving major advancements in data acquisition technology [30, 34, 35]. In decay experiments, DDAQ systems enable processing at higher rates with reduced dead time. Furthermore, digital pulse processing techniques have been employed to record raw signal waveforms, resolve pile-up events [36], and distinguish between different charged particles, such as α particles and protons.

The nucleus ^{32}Ar and its decay [37–43], with an isospin projection of $T_Z = -2$, have been extensively studied, providing a reliable benchmark for testing the performance of the new detection system. An experiment conducted at ISOLDE [40] observed protons emitted from the isobaric analog state (IAS) and verified the isobaric multiplet mass equation (IMME). Another study [41] focused primarily on the giant Gamow–Teller (GT) resonance. Schardt and Riisager [37] examined the limits of exotic currents in weak interactions. The decay strength and *ft* value for the superallowed β decay of ^{32}Ar were experimentally determined by Bhattacharya et al. [42], enabling the deduction of the isospin-impurity correction, δ_C. Recent work at GANIL [43] further investigated the Fermi strength and GT strength distributions in the decay of ^{32}Ar, comparing the experimental results with predictions from the shell model.

In this study, we focused on the design and performance evaluation of a detector array comprising DSSDs, quadrant silicon detectors (QSDs), and germanium detectors for high-precision measurements of β-decay spectroscopy in proton-rich nuclei within the *sd*-shell region. An advanced DDAQ system, based on the Pixie-16 module developed by XIA LLC [44], was employed during the experiments. Section 2 describes the detector array configuration and the DAQ system, and particle identification capabilities demonstrated in the in-beam test. The detector responses to charged particles and γ-rays obtained during offline testing are detailed in Sect. 3. Experimental results showcasing high-precision measurements of the β decay of ^{32}Ar, as an application of the detection system, are presented in Sect. 4. Finally, a summary of the study is provided.

2 Experimental setup

2.1 In-beam test

The performance of the detection system was evaluated using the β-delayed proton emitter ^{32}Ar at the first Radioactive Ion Beam Line in Lanzhou (RIBLL1) [45]. A K450 separate sector cyclotron (SSC) provided a 69.44 MeV/u primary beam of $^{36}Ar^{18+}$ with an intensity of ~87 enA. The secondary beam was generated via projectile fragmentation of the ^{36}Ar primary beam on a 1000 μm thick ^{9}Be target. The average intensity and purity of ^{32}Ar in the secondary beam delivered to the detection chamber had an average intensity of 0.61 particles per second (pps) and a purity of 0.086%. Data collection for ^{32}Ar spanned 17.8 h. The ^{32}Ar ions were separated and purified by the RIBLL1 facility and identified through energy loss (ΔE) and time-of-flight (TOF) measurements. The TOF was determined using two plastic scintillation detectors positioned at the two focal planes of RIBLL1. Particle identification and beam optimization were carried out using LISE++ simulations [46] and calibration using secondary beams. Upstream of the detector setup, following the two plastic scintillators (T_1 and T_2), a series of aluminum foils operated by three stepping motors were installed as energy degraders. The thickness of the aluminum degraders could be finely adjusted in small increments of 5 μm, with a full range of 315 μm, enabling precise tuning of the stopping range for ^{32}Ar ions within the DSSDs. A total of 3.9×10^4 ^{32}Ar ions were implanted into DSSD1 and DSSD2, with implantation proportions of 82.2% and 17.8%, respectively.

A two-dimensional identification plot of ΔE versus TOF for the implanted ions is shown in Fig. 2, demonstrating the system's ability to effectively distinguish among nuclei such as ^{32}Ar, ^{31}Cl, ^{30}S, and ^{29}P.

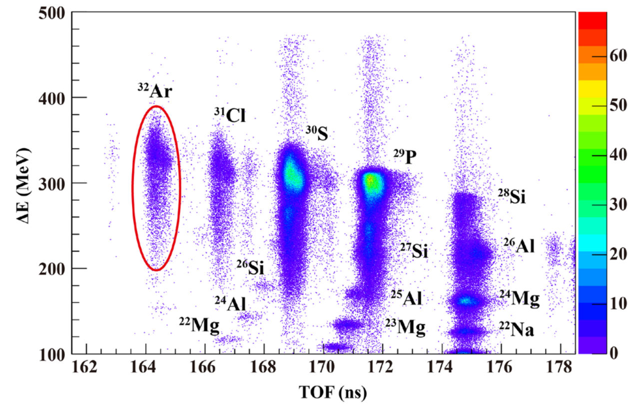

Fig. 2 (Color online) Two-dimensional identification plot of ΔE versus TOF for the ions in the secondary beam is shown. The horizontal axis represents the time difference between scintillators T1 and T2, while the vertical axis corresponds to the energy loss in the SDΔE2 detector. An additional coincidence gating condition based on the energy loss in the QSDΔE1 detector is applied to enhance the identification

2.2 Detector array

A schematic of the detection setup is shown in Fig. 1. The two silicon detectors positioned in front of the silicon array facilitated the measurement of ΔE. The ΔE values of the secondary beam were provided by a 300-μm-thick quadrant silicon detector (QSDΔE1) and a 150-μm-thick silicon detector (SDΔE2). These two ΔE detectors, positioned sequentially along the beamline, allowed the continuous monitoring of the beam composition throughout the experiment. The ΔE-TOF correlation served as a powerful tool for particle

Fig. 1 (Color online) Schematic layout of the detection system (not to scale)

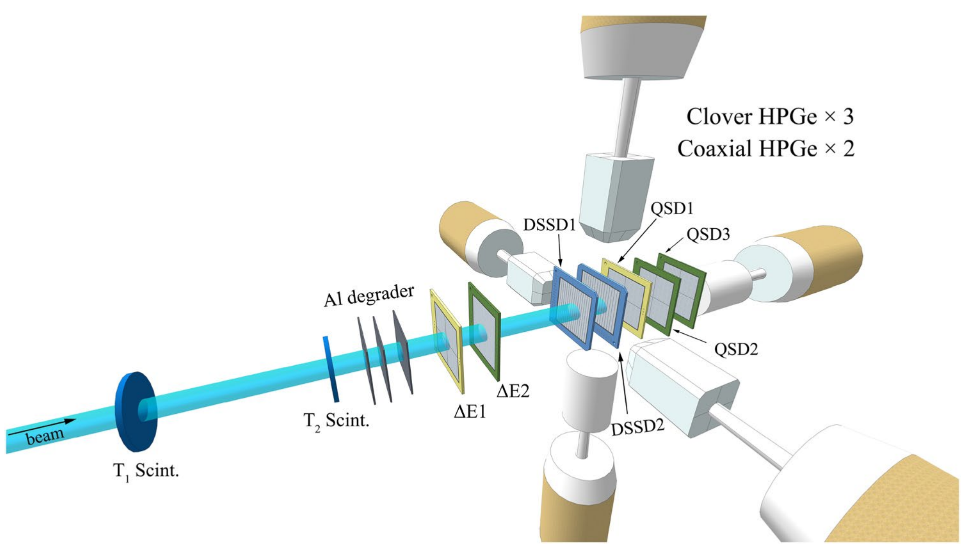

identification [13]. The secondary ions of interest were implanted into a silicon array surrounded by high-purity germanium (HPGe) detectors manufactured by Canberra [47] to study their decay properties. A 50-µm-thick DSSD1 (W1-type from Micron Semiconductor Ltd. [48]) was used to stop the isotopes of interest and simultaneously functioned as a detector for β-delayed proton decays. Additionally, a 300-µm DSSD2 (W1-type) serving a similar role was positioned 10 mm downstream of DSSD1. A thinner DSSD is aimed at detecting low-energy protons with a reduced β particle background, given that the β particles extend over a longer range in silicon. DSSD2 has a higher detection efficiency for high-energy protons, which is an important supplement to the thinner DSSD1. Furthermore, the two DSSDs could detect protons emitted from one detector to another. Placed downstream from DSSD2, QSD1 with a thickness of 1500 µm acted as a veto detector for penetrating heavy ions and detected protons escaping from DSSD2. Subsequently, at the end of the silicon array, QSD2 and QSD3 with thicknesses of 300 µm were positioned downstream to reduce the potential disturbances from the penetrating light particles (^{1}H, ^{2}H, ^{3}H, ^{4}He) coming along with the secondary beam. The active area of each silicon detector is 50 mm × 50 mm. Surrounding the silicon chamber, three clover-type HPGe detectors and two coaxial-type HPGe detectors were installed to measure the γ rays produced during the decay of the implanted nuclei.

All silicon detectors in this setup were mounted on printed circuit boards (PCBs) and paired with SPA02-type preamplifiers [49]. To optimize resolution and ensure operational stability, the silicon detectors and preamplifiers were maintained at a temperature range of approximately −2 °C to 5 °C, using a circulating cooling alcohol system. Signals from the silicon and HPGe detectors were directly processed by a Pixie-16 digitizer, which employed real-time algorithms for energy and timing analysis.

2.3 Digital data acquisition system

The DDAQ system consists of a crate, several Pixie-16 modules from XIA LLC [44], a crate controller module, and a trigger module. The primary component is the Pixie-16 6U CompactPCI/PXI crate, which accommodates additional plug-in units, provides localized power, and facilitates communication of digital signals between units. Additionally, a PCI-8366/PXI-8368 crate controller is included, serving as the commander for the other modules and enabling communication with the computer via fiber optic cable. The computer sends commands to the DAQ system and retrieves data from the memory of the modules through the crate controller, at a rate of up to 109 MByte/s.

The Pixie-16 modules serve as digitizers, converting analog signals into digital data using a 12/14/16-bit ADC at sampling rates of 100/250/500 MHz. Seven 250 MHz Pixie-16 modules with 14-bit ADCs were employed in this experiment. The ohmic and junction sides of two 16×16 DSSDs were connected to four modules with 64 channels, while the remaining detectors were connected to the other three modules. These modules derive energy and time information from the input signal based on a predefined algebraic formula [50]. The Pixie-16 module combines the functions of a shaping amplifier, discriminator, ADC, and TDC, typically found in traditional DAQ systems. The programmable MicroZed-based trigger I/O (MZTIO) [51] module acts as the logic trigger component, routing signals between the PXI backplane and crate front panel and creating logical combinations within a field-programmable gate array (FPGA) chip. Synchronization of different crates is achieved using the Pixie-16 clock and the trigger I/O module. Further details on the technical implementation, including clock synchronization and trigger distribution between separate crates, can be found in [52, 53]. Figure 3 shows a photograph of a typical digital data acquisition system.

Detector signals were initially digitized using the Pixie-16, with subsequent signal processing performed by a set of real-time algorithms in the firmware. When a physical event is detected via local or external triggers, its data are first saved in the FPGA's local memory and then transferred to an external first-in, first-out (FIFO) memory [54]. Data in the FIFO are sent to the host computer via a fiber optic cable and then transmitted to the data storage center. Parameters such as the rise and flat-top times of the trapezoidal filter are set through a graphical user interface (GUI) using specific algorithms derived from digital signal processing (DSP). The trigger and energy filter parameters for the rise and flat-top times in the present experiment are listed in Table 1. An internal or external trigger can be selected from the DDAQ

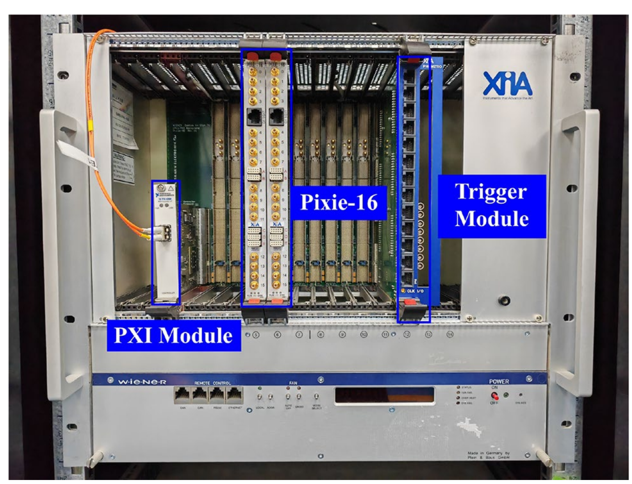

Fig. 3 (Color online) Depiction of the data acquisition system

Table 1 Trigger and energy filter parameter settings for the rise and flat-top times of this experiment

Parameter	Detector type	
	Silicon	HPGe
Trigger T_{rise} (μs)	0.104	0.104
Trigger T_{flat} (μs)	0	0.104
Energy T_{rise} (μs)	3.040	5.506
Energy T_{flat} (μs)	0.256	1.600
τ (μs)	150	50

system. For the internal trigger, a specific threshold was established for the Pixie-16 modules. The multiplicity and/or coincidence in each Pixie-16 module or between modules were determined using the system FPGA [34]. A programmable MZTIO module was used to implement efficient and flexible trigger patterns for external triggers. The MZTIO module is based on a custom carrier board and a commercial MicroZed Zynq processor module, which combines an FPGA fabric (for trigger logic) and an ARM processor (running Linux) on the same chip. All Zynq firmware and software packages were customized for DDAQ [55]. The external triggering mechanism was implemented as follows: The multiplicity triggers extracted from each selected channel in the immediately neighboring Pixie-16 modules were sent to the low-voltage differential signaling (LVDS) inputs of the MZTIO through the RJ45 connectors. Subsequently, a corresponding trigger signal, called a "valid trigger", based on user-defined logic, was generated and sent back as a module validation trigger for the Pixie-16 modules.

With the powerful trigger logic system of DDAQ [56], complex logic operations of signals from different detectors can be easily implemented. An example of trigger generation is provided in the literature [55]. The trigger system used in the experiment is shown in Fig. 4. The logic trigger signals for the two DSSDs were generated by the coincident

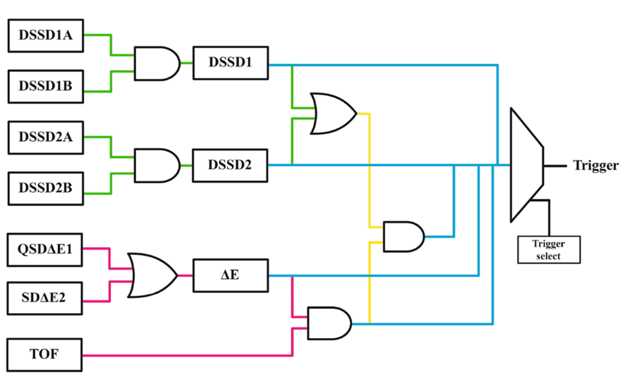

Fig. 4 Schematic of the main logic trigger generation for detectors is shown. A and B represent the ohmic and junction sides of the DSSD, respectively. For further details, refer to the text

signals between the junction and the ohmic sides. After passing through the analog constant-fraction discriminator (CFD) module ORTEC 935 [57], the signals from the two plastic scintillator detectors were converted using a time-to-amplitude converter (TAC) to obtain the TOF signal. The ΔE detectors were triggered by a logical OR operation between the QSDΔE1 and SDΔE2 detectors. The trigger signal was delayed to align with the TOF signal and stretched to a width of approximately 500 ns.

To better suppress the trigger rate, the ΔE detectors can also be triggered by the valid coincidence signals between the ΔE-TOF and DSSD signals (yellow line). All trigger signals were sent to and configured in the MZTIO module. The other QSDs and Ge detectors used in this experiment were self-triggered to capture the signals.

3 offline and in-beam performance

A ^{239}Pu-^{241}Am-^{244}Cm triple-α source was used for preliminary energy calibration of the DSSDs and QSDs. The primary peak energies of the triple-α source were 5157, 5486, and 5805 keV. Energy calibration was conducted independently for each strip before analysis. Using a linear calibration model, $E(x) = ax + b$, where x represents the ADC channel number, the coefficient a exhibited fluctuations of less than 5% across all strips, while b shifted by less than 1% of the full energy range (10 MeV). The energy spectra obtained from the pixels of the 10th junction strip and the 10th ohmic strip in DSSD2 are shown in Fig. 5. Constrained by the energy resolution of the detector, a low-energy tail emerges due to contamination of the primary peak by non-primary peaks. For example, the principal α-decay paths of ^{239}Pu are 5157

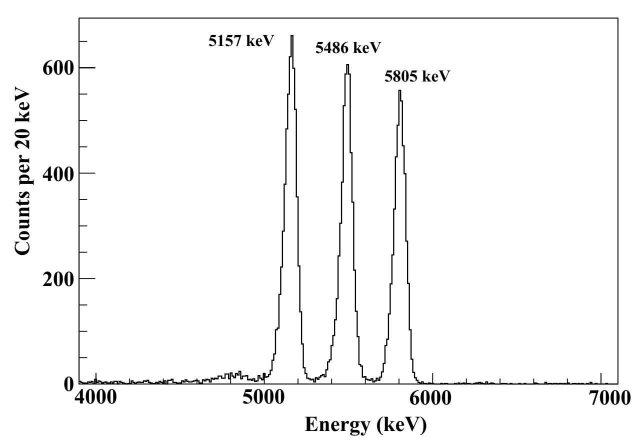

Fig. 5 α energy spectrum for the pixel in the 10th junction strip and the 10th ohmic strip is presented. By applying a Gaussian fit to the 5157 keV peak, the junction strip yields an energy resolution of 71 keV (FWHM)

keV (71%), 5144 keV (17%), and 5106 keV (12%) [58]. The results obtained from the Gaussian fit indicate that for the 5157 keV energy peak, the energy resolutions of both the junction and the ohmic strips are approximately 70 keV (FWHM). The formal energy calibration of the DSSDs was performed using known β-delayed protons from ^{25}Si [59] and ^{29}S [60] decay during the experiment. This calibration provides more reliable energy measurements as it does not require additional corrections, such as for the incident angle of the particle or the thickness of the dead layer.

To evaluate the detection efficiency of the DSSDs for β-delayed protons in the decay process, the Monte Carlo simulation was applied. In the simulation, protons were set to be emitted isotropically from various random positions given by the distributions of the ion stopping positions. The peak area of each proton group in the β-delayed proton spectra can be corrected according to the efficiency distributions to extract the true count for the intensity determination. The distribution of the implantation depth (z distribution) can be deduced from the SRIM calculation [61] using the energy-loss distributions. The detection efficiencies of the DSSDs were experimentally determined based on the known intensities of β-delayed protons from ^{29}S, which were found to be in good agreement with the simulation results shown in Fig. 6.

Energy and efficiency calibrations of the HPGe detectors were performed using ^{152}Eu [62] and ^{133}Ba [63] sources. The detection efficiencies of the standard sources are as follows:

$$\varepsilon = \frac{N_{\mathrm{det}}}{N}, \tag{1}$$

where N_{det} is the count of γ rays with a certain energy measured by the HPGe detectors, and N is the count of γ rays emitted by the standard γ source. N can be calculated using the following expression:

$$N = N_0 e^{-\lambda T} \cdot \mathrm{d}t \cdot I_\gamma, \tag{2}$$

where $N_0 e^{-\lambda T}$ is the activity of the standard γ source, T is the time from the production of the source to the experiment, $\mathrm{d}t$ is the counting time, and I_γ is the branching ratio of the standard γ sources, as shown in Table 2 extracted from Ref. [62, 63]. The activities $N_0 e^{-\lambda T}$ of ^{152}Eu and ^{133}Ba sources were 181 ± 10% kBq and 120 ± 10% kBq, respectively.

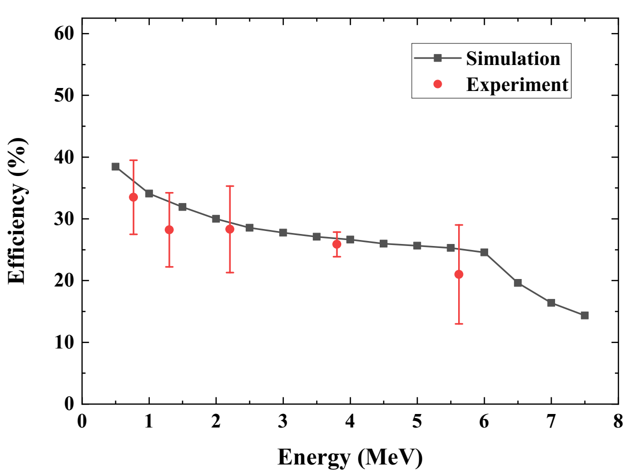

Fig. 6 Simulated and experimental detection efficiencies for β-delayed protons as a function of the proton energy in DSSD2

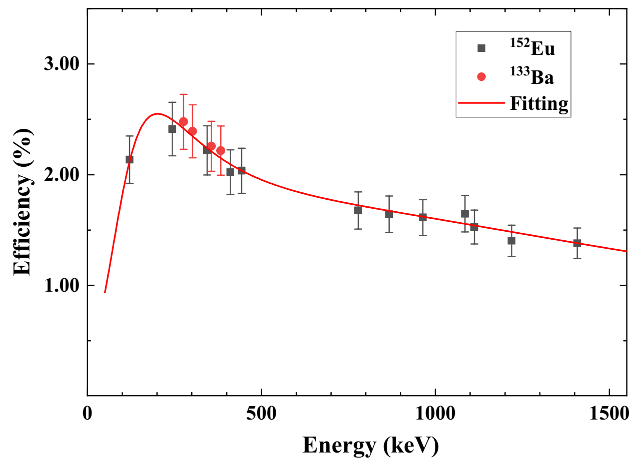

Fig. 7 Absolute detection efficiency of the HPGe detectors for γ rays from standard sources as a function of energy. Details are provided in the text

Table 2 Standard γ ray sources and the energies and intensities of their rays (I_γ)

Source	Energies (keV)	Intensities (%)
^{152}Eu	121.7817	28.53
	244.6974	7.55
	344.2785	26.59
	411.1165	2.237
	443.9606	2.827
	778.9045	12.93
	867.380	4.23
	964.057	14.51
	1085.837	10.11
	1112.076	13.67
	1212.948	1.415
	1408.013	20.87
^{133}Ba	276.3989	7.16
	302.8508	18.34
	356.0129	62.05
	383.8485	8.94

The intrinsic detection efficiency of the Ge detectors can be expressed using the following equation [64]:

$$\ln(\varepsilon) = \{(A + Bx + Cx^2)^{-G} + (D + Ey + Fy^2)^{-G}\}^{-\frac{1}{G}}, \quad (3)$$

where $x = \ln(E_\gamma/100[\mathrm{keV}])$, $A + Bx + Cx^2$ is applicable to the low-energy region; $y = \ln(E_\gamma/1000[\mathrm{keV}])$, $D + Ey + Fy^2$ is applicable to the high-energy region; G represents the interaction parameter between the high and low-energy components. The uncertainty in the full-energy peak efficiency shown in Fig. 7 was calculated by considering the peak fitting uncertainty and activity uncertainties of the sources. The total efficiency and energy resolution for registering γ rays at 1112 keV were estimated to be 1.52(15)% and 3.3 keV (FWHM), respectively.

4 Results and discussion

The detection of β-delayed proton decay events required a signal above the fast trigger threshold in the two DSSDs while simultaneously rejecting coincidence signals within the ΔE-TOF gate. To further suppress noise and background, the energy difference between decay signals from the junction side strips and the ohmic side strips was constrained to within $\pm 10\%$ of the signal value or no more than ± 100 keV. Additionally, x–y pixel position information from the DSSDs was utilized to correlate ion implantation events with subsequent decay events. Each x–y pixel of the DSSD effectively acts as an independent detector, enabling the implantation rate per pixel to remain low. This design allows for a higher overall implantation rate in the DSSD, even in continuous-beam mode.

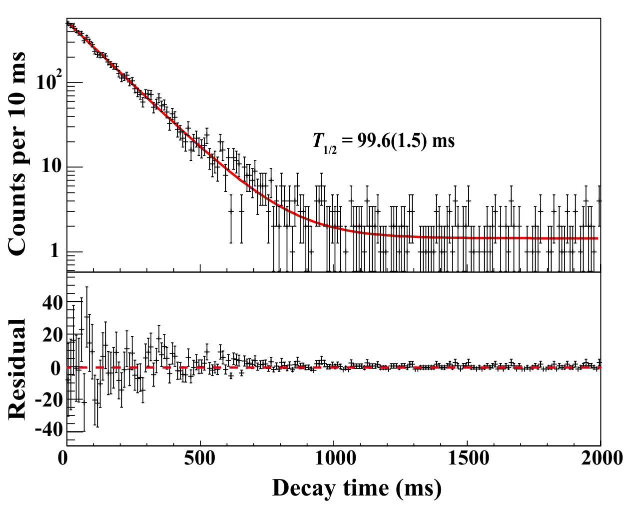

Fig. 8 Decay-time spectrum of ^{32}Ar is shown at the top and residuals between experimental data and the fitting curve are shown at the bottom

The time difference between an implantation event and all subsequent decay events occurring in the same x–y pixel of the DSSD is defined as the correlation time. As shown in Fig. 8, the decay-time spectrum of ^{32}Ar is obtained by summing the correlation times from all pixels in DSSD2. To reduce the influence of background at low energies, only decay events with energies above 800 keV in the DSSDs are considered. The decay-time spectrum includes a small number of random correlations, where implantation events are accidentally paired with decay events from other implantations or background disturbances. True correlated implantation–decay event pairs follow an exponential distribution, while uncorrelated pairs contribute a constant background. The fitting expression is as follows:

$$N(t) = He^{-\frac{t\ln 2}{T_{1/2}}} + I, \quad (4)$$

where $N(t)$ represents the total number of ions decaying as a function of time t, H is the number of ions decaying initially, I is the constant background, and $T_{1/2}$ is the half-life of the isotope. From the fit to the decay-time spectrum, the half-life of ^{32}Ar was determined to be $T_{1/2} = 99.6 \pm 1.5$ ms, where the uncertainty includes both statistical errors and the fitting uncertainty. This result is in excellent agreement with previous measurements, as summarized in Table 3.

Table 3 Half-life values for ^{32}Ar

Literature	$T_{1/2}$ (ms)
Hagberg [40]	75^{+70}_{-30}
Björnstad [41]	98(2)
ISOLDE [42]	100.5(3)
Present work	99.6(15)

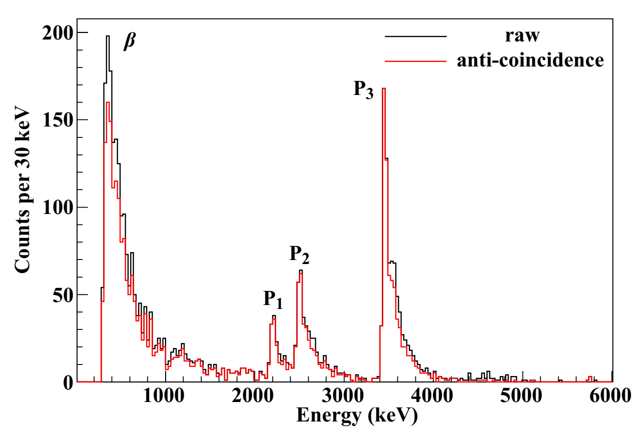

Fig. 9 β-delayed proton spectrum from the β decay of ^{32}Ar, measured by DSSD2, is shown in the figure. Each proton peak originating from the β-delayed proton decay of ^{32}Ar is labeled with a letter "P" followed by a number. The black line represents the raw spectrum measured by DSSD2, while the red line indicates the energy spectrum vetoed by QSD1

Table 4 Intensities for β-delayed proton

Peaks	Proton energies (keV)	Intensities (%)	
		Present work	Previous work [43]
P_1	2212(5)	4.0(5)	3.62(7)
P_2	2503(4)	6.2(7)	7.24(11)
P_3	3470(5)	20.8(12)	20.51(17)

The β-delayed proton spectrum from the decay of ^{32}Ar, measured by DSSD2, is shown in Fig. 9. Each proton peak in the spectrum is labeled with a letter "P" followed by a number, corresponding to distinct proton emission events from the β-delayed proton decay of ^{32}Ar. To ensure accurate decay event detection, the time difference between an implantation event and subsequent decay events was limited to approximately six half-lives (600 ms). Disturbances from penetrating heavy ions and light particles were effectively eliminated through anticoincidence with veto detectors QSD1, QSD2, and QSD3. The origin of each proton peak was identified through half-life analysis. Three distinct proton peaks were observed, and the corresponding peak intensities are summarized in Table 4.

The intensities of β-delayed protons can be determined using the following equation:

$$I_{\beta p} = \frac{N_{\mathrm{p}}}{\varepsilon_{\beta p} \cdot N_{\mathrm{imp}}}, \tag{5}$$

where $I_{\beta p}$ is the intensity of the decay branch, N_{p} represents the number of β-delayed proton decay events measured by the DSSD, $\varepsilon_{\beta p}$ is the β-delayed proton detection efficiency, calibrated using β-delayed protons from ^{29}S in the subsequent stage of the experiment, and N_{imp} is the total number of implanted ^{32}Ar ions. Background correction is performed using the correlation time to remove background contributions from β-particles or other accidental disturbances. Thanks to the waveform digitization capability and the trigger rate employed in this experiment, it is reasonable to assume that all triggered events were successfully recorded. Consequently, unlike traditional data acquisition systems, dead-time correction was not necessary in this experiment. The intensities of each proton group obtained in the present study are in good agreement with those from previous work [43]. The overall uncertainties include both calibration parameter uncertainties and peak-energy Gaussian fitting uncertainties.

Due to the relatively low statistics, no β-delayed γ rays from the decay of ^{32}Ar were observed in the present experiment. However, the β-delayed γ rays from the decay of ^{30}S, which had higher implantation counts, are shown in Fig. 10 to demonstrate the measurement capability of the system. Statistically, the significant peak in the spectrum is the well-known 511-keV γ ray, originating from positron-electron annihilation. The 677-keV γ ray is assigned to the de-excitation from the first 0^+ excited state to the ground state of ^{30}P. Its intensity was determined to be 74(5)%, which is in good agreement with the literature value of 78.4(4)% [65]. After a γ-γ coincidence check, the 1368-keV and 2754-keV γ rays were likely due to ^{24}Mg contaminants from the decay of ^{24}Al. The inset of Fig. 10 shows the two γ rays from the β decay of ^{31}Cl, despite the low implantation counts. The 1248-keV and 2234-keV γ rays are assigned to the de-excitation from the two lowest excited states to the ground state of ^{31}S.

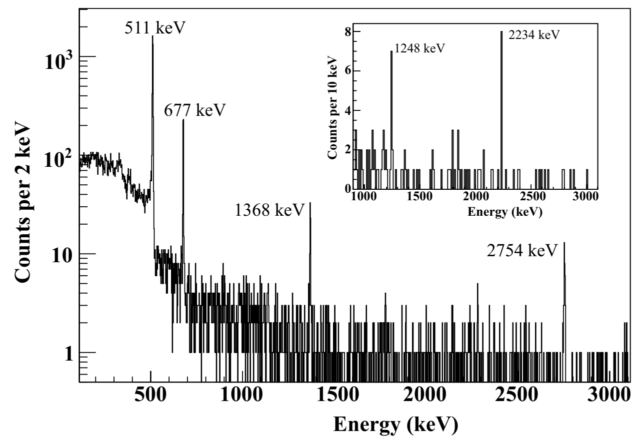

Fig. 10 Cumulative γ-ray spectrum measured by the HPGe detectors in coincidence with the β particles from the decay of ^{30}S, as recorded by DSSD2, is shown. The inset displays the partial γ-ray spectrum in coincidence with the β particles from the decay of ^{31}Cl. The γ-ray peaks are labeled with their respective energies

Additionally, the proposed detection system can be applied to measure other exotic decay modes. Further improvements and methods are under consideration, including the use of pulse shape discrimination (PSD) for silicon detectors, which can be applied to identify different charged particles using the DDAQ system.

5 Conclusion

A novel decay detection system utilizing an implantation method with a digital data acquisition system was developed and commissioned for the experiment on β-delayed proton decay of ^{32}Ar in continuous-beam mode. This setup enabled accurate identification of the implanted nuclei and subsequent decays through energy, time, and position measurements. Although the collection time in our experiment was much shorter than in previous studies of ^{32}Ar, a relatively high number of decay events were accumulated, and reliable results were obtained due to our enhanced experimental techniques. It would be beneficial to extract more information from future experiments with improved statistics. The detection system demonstrated its effectiveness in measuring β-delayed proton decay, and further research can be extended to studying more exotic decay modes.

Acknowledgements We wish to acknowledge the support of the HIRFL operations staff for providing high-quality beams and the efforts of the RIBLL1 collaborators in performing the experiment.

Author contributions All authors contributed to the study conception and design. Material preparation, data collection and analysis were performed by Hao Jian, Xin-Xing Xu, Kai-Long Wang, Jia-Jian Liu, Chao-Yi Fu, Peng-Jie Li, Yan-Yun Yang, Guang-Xin Zhang, Kang Wang, Fang-Fang Duan, Long-Hui Ru, Guang-Shun Li, Bing Ding, Yun-Hua Qiang, Cen-Xi Yuan, Jun-Bing Ma, Shi-Wei Xu, Yu-Feng Gao, Rui Fan, Fan-Chao Dai, Si-Xian Zha, Hao-Fan Zhu, Jin-Hai Li, Shu-Lian Qin, Zhi-Fang Chang, Cheng Kong, He-Xuan Yan, Hao-Wei Xu, Jia-Long Ning, Bo-Ren Liu, Jie Zhou, Yu-Dong Chen, Bo-Shuai Cai, Yu-Ting Wang, Hong-Yi Wu, Zhi-Xuan Wang, Dong-Sheng Hou, Hu-Shan Xu, Xiao-Hong Zhou, Yu-Hu Zhang, Meng Wang, Zheng-Guo Hu, and Jenny Lee. The first draft of the manuscript was written by Hao Jian, and all authors commented on previous version of the manuscript. All authors read and approved the final manuscript.

Data availibility The data that support the findings of this study are openly available in Science Data Bank at https://cstr.cn/31253.11.sciencedb.j00186.00539 and https://doi.org/10.57760/sciencedb.j00186.00539.

Declarations

Conflict of interest The authors declare that they have no conflict of interest.

References

1. B. Blank, M.J.G. Borge, Nuclear structure at the proton drip line: advances with nuclear decay studies. Prog. Part. Nucl. Phys. **60**, 403 (2008). https://doi.org/10.1016/j.ppnp.2007.12.001
2. M.J.G. Borge, Beta-delayed particle emission. Physica Scripta **T152**, 014013 (2013). https://doi.org/10.1088/0031-8949/2013/T152/014013
3. M. Pfützner, M. Karny, L.V. Grigorenko et al., Radioactive decays at limits of nuclear stability. Rev. Mod. Phys. **84**, 567 (2012). https://doi.org/10.1103/RevModPhys.84.567
4. K. Miernik, W. Dominik, Z. Janas et al., Two-proton correlations in the decay of ^{45}Fe. Phys. Rev. Lett. **99**, 192501 (2007). https://doi.org/10.1103/PhysRevLett.99.192501
5. P. Ascher, L. Audirac, N. Adimi et al., Direct observation of two protons in the decay of ^{54}Zn. Phys. Rev. Lett. **107**, 102502 (2011). https://doi.org/10.1103/PhysRevLett.107.102502
6. J. Bishop, G.V. Rogachev, S. Ahn et al., First observation of the $\beta3\alpha p$ decay of ^{13}O via β-delayed charged-particle spectroscopy. Phys. Rev. Lett. **130**, 222501 (2023). https://doi.org/10.1103/PhysRevLett.130.222501
7. R. Mahajan, T. Wheeler, E. Pollacco et al., Time projection chamber for GADGET II. Phys. Rev. C **110**, 035807 (2024). https://doi.org/10.1103/PhysRevC.110.035807
8. A.A. Ciemny, C. Mazzocchi, W. Dominik et al., β-delayed charged-particle decay of ^{22,23}Si. Phys. Rev. C **106**, 014317 (2022). https://doi.org/10.1103/PhysRevC.106.014317
9. N. Larson, S.N. Liddick, M. Bennett et al., High efficiency beta-decay spectroscopy using a planar germanium double-sided strip detector. Nucl. Instrum. Meth. Phys. A **727**, 59–64 (2013). https://doi.org/10.1016/j.nima.2013.06.027
10. B. Blank, A. Bey, G. Canchel, C. Dossat et al., First observation of ^{54}Zn and its decay by two-proton emission. Phys. Rev. Lett. **94**, 232501 (2005). https://doi.org/10.1103/PhysRevLett.94.232501
11. C. Dossat, A. Bey, B. Blank et al., Two-proton radioactivity studies with ^{45}Fe and^{48Ni}. Phys. Rev. C **72**, 054315 (2005). https://doi.org/10.1103/PhysRevC.72.054315
12. J. Giovinazzo, B. Blank, M. Chartier et al., Two-proton radioactivity of ^{45}Fe. Phys. Rev. Lett. **89**, 102501 (2002). https://doi.org/10.1103/PhysRevLett.89.102501
13. L.J. Sun, X.X. Xu, C.J. Lin et al., β-decay spectroscopy of ^{27}S. Phys. Rev. C **99**, 064312 (2019). https://doi.org/10.1103/PhysRevC.99.064312
14. G.Z. Shi, J.J. Liu, Z.Y. Lin et al., β-delayed two-proton decay of ^{27}S at the proton-drip line. Phys. Rev. C **103**, L061301 (2021). https://doi.org/10.1103/PhysRevC.103.L061301
15. P.F. Liang, L.J. Sun, J. Lee et al., Simultaneous measurement of β-delayed proton and γ emission of ^{26}P for the ^{25}Al(p, γ) ^{26}Si reaction rate. Phys. Rev. C **101**, 024305 (2020). https://doi.org/10.1103/PhysRevC.101.024305
16. H. Jian, Y.F. Gao, F.C. Dai et al., β-delayed γ emissions of ^{26}P and its mirror asymmetry. Symmetry **13**, 2278 (2021). https://doi.org/10.3390/sym13122278
17. J.J. Liu, X.X. Xu, L.J. Sun et al., Observation of a strongly isospin-mixed doublet in ^{26}Si via β-delayed two-proton decay of ^{26}P. Phys. Rev. Lett. **129**, 242502 (2022). https://doi.org/10.1103/PhysRevLett.129.242502
18. X.X. Xu, C.J. Lin, L.J. Sun et al., Observation of β-delayed two-proton emission in the decay of ^{22}Si. Phys. Lett. B **766**, 312–316 (2017). https://doi.org/10.1016/j.physletb.2017.01.028
19. J. Lee, X.X. Xu, K. Kaneko et al., Large isospin asymmetry in ^{22}Si/^{22}O mirror Gamow-Teller transitions reveals the halo structure of ^{22}Al. Phys. Rev. Lett. **125**, 192503 (2020). https://doi.org/10.1103/PhysRevLett.125.192503
20. Y.T. Wang, D.Q. Fang, K. Wang et al., Observation of β-delayed ^{2}He emission from the proton-rich nucleus ^{22}Al. Phys. Lett. B **784**, 12–15 (2018). https://doi.org/10.1016/j.physletb.2018.07.034
21. Y.T. Wang, D.Q. Fang, X.X. Xu et al., Implantation-decay method to study the β-delayed charged particle decay. Nucl. Sci. Tech. **29**, 98 (2018). https://doi.org/10.1007/s41365-018-0438-5
22. C.G. Wu, H.Y. Wu, J.G. Li et al., β-decay spectroscopy of the proton drip-line nucleus ^{22}Al. Phys. Rev. C **104**, 044311 (2021). https://doi.org/10.1103/PhysRevC.104.044311
23. Y.T. Wang, D.Q. Fang, K. Wang et al., β-delayed particle emission from ^{21}Mg. Eur. Phys. J. A **54**, 107 (2018). https://doi.org/10.1140/epja/i2018-12543-1
24. K. Wang, D.Q. Fang, Y.T. Wang et al., Spectroscopic study of β -delayed particle emission from proton-rich nucleus ^{23}Si. Inter. J. Mod. Phys. E **27**, 1850014 (2018). https://doi.org/10.1142/S0218301318500143
25. R.V. Ribas, A camac data acquisition system based on PC-Linux. Nucl. Instrum. Meth. Phys. A **483**, 830–832 (2002). https://doi.org/10.1016/S0168-9002(01)01950-7
26. T. Prokscha, R. Scheuermann, U. Hartmann et al., A novel VME based μSR data acquisition system at PSI. Phys. B Cond. Matter **404**, 1007–1009 (2009). https://doi.org/10.1016/j.physb.2008.11.206

27. H. Baba, T. Ichihara, T. Ohnishi et al., New data acquisition system for the RIKEN Radioactive Isotope Beam Factory. Nucl. Instrum. Meth. Phys. A **616**, 65–68 (2010). https://doi.org/10.1016/j.nima.2010.02.120
28. R. Grzywacz, Applications of digital pulse processing in nuclear spectroscopy. Nucl. Instrum. Meth. Phys. B **204**, 649–659 (2003). https://doi.org/10.1016/S0168-583X(02)02146-8
29. A. Al-Adili, F.-J. Hambsch, S. Oberstedt et al., Comparison of digital and analogue data acquisition systems for nuclear spectroscopy. Nucl. Instrum. Meth. Phys. A **624**, 684–690 (2010). https://doi.org/10.1016/j.nima.2010.09.126
30. C.J. Prokop, S.N. Liddick, B.L. Abromeit et al., Digital data acquisition system implementation at the national superconducting cyclotron laboratory. Nucl. Instrum. Meth. Phys. A **741**, 163–168 (2014). https://doi.org/10.1016/j.nima.2013.12.044
31. M.J. Koskelo, I.J. Koskelo, B. Sielaff, Comparison of analog and digital signal processing systems using pulsers. Nucl. Instrum. Meth. Phys. A **422**, 373–378 (1999). https://doi.org/10.1016/S0168-9002(98)00986-3
32. S. Mitra, L. Wielopolski, G. Hendrey, Comparison of a digital and an analog signal processing system for neutron inelastic gamma-ray spectrometry. Appl. Radiat. Isotop. **61**, 1463–1468 (2004). https://doi.org/10.1016/j.apradiso.2004.02.024
33. J. Kamleitner, S. Coda, S. Gnesin et al., Comparative analysis of digital pulse processing methods at high count rates. Nucl. Instrum. Meth. Phys. A **736**, 88–98 (2014). https://doi.org/10.1016/j.nima.2013.10.023
34. D.W. Luo, H.Y. Wu, Z.H. Li et al., Performance of digital data acquisition system in gamma-ray spectroscopy. Nucl. Sci. Tech. **32**, 79 (2021). https://doi.org/10.1007/s41365-021-00917-8
35. A. Harter, M. Weinert, L. Knafla et al., Systematic investigation of time walk and time resolution characteristics of CAEN digitizers V1730 and V1751 for application to fast-timing lifetime measurement. Nucl. Instrum. Meth. Phys. A **1053**, 168356 (2023). https://doi.org/10.1016/j.nima.2023.168356
36. X. Wang, Z.H. Li, Z. Liu et al., An effective digital pulse processing method for pile-up pulses in decay studies of short-lived nuclei. Nucl. Instrum. Meth. Phys. A **971**, 164068 (2020). https://doi.org/10.1016/j.nima.2020.164068
37. D. Schardt, K. Riisager, Beta-neutrino recoil broadening in β-delayed proton emission of ^{32}Ar and ^{33}Ar. Z. Physik A - Hadrons and Nuclei **345**, 265–271 (1993). https://doi.org/10.1007/BF01280833
38. E.G. Adelberger, C. Ortiz, A. García et al., Positron-neutrino correlation in the $0^+ \rightarrow 0^+$ decay of ^{32}Ar. Phys. Rev. Lett. **83**, 1299 (1999). https://doi.org/10.1103/PhysRevLett.83.1299
39. V. Araujo-Escalona, D. Atanasov, X. Fléchard et al., Simultaneous measurements of the β-neutrino angular correlation in ^{32}Ar pure Fermi and pure Gamow-Teller transitions using β-proton coincidences. Phys. Rev. C **101**, 055501 (2020)
40. E. Hagberg, P.G. Hansen, J.C. Hardy et al., Decay of a $T_z = -2$ nucleus: Argon-32. Phys. Rev. Lett. **39**, 792–795 (1977). https://doi.org/10.1103/PhysRevLett.39.792
41. T. Björnstad, M.J.G. Borge, P. Dessagne et al., Study of the giant gamow-teller resonance in nuclear β-decay: the case of ^{32}Ar. Nucl. Phys. A **443**, 283–301 (1985). https://doi.org/10.1016/0375-9474(85)90264-7
42. M. Bhattacharya, D. Melconian, A. Komives et al., *ft* value of the $0^+ \rightarrow 0^+$ β^+ decay of ^{32}Ar: a measurement of isospin symmetry breaking in a superallowed decay. Phys. Rev. C **77**, 065503 (2008). https://doi.org/10.1103/PhysRevC.77.065503
43. B. Blank, N. Adimi, M. Alcorta et al., Detailed study of the decay of ^{32}Ar. Eur. Phys. J. A **57**, 28 (2021). https://doi.org/10.1140/epja/s10050-020-00341-3
44. XIA LLC, https://xia.com/
45. Z. Sun, W.L. Zhan, Z.Y. Guo et al., RIBLL, the radioactive ion beamline in Lanzhou. Nucl. Instrum. Meth. Phys. Res. A **503**, 496–503 (2003). https://doi.org/10.1016/S0168-9002(03)01005-2
46. O.B. Tarasov, D. Bazin, LISE++: radioactive beam production with in-flight separators. Nucl. Instrum. Meth. Phys. B **266**, 4657–4664 (2008). https://doi.org/10.1016/j.nimb.2008.05.110
47. Germanium detectors, Mirion Technologies (Canberra) Inc. https://www.mirion.com/products/technologies/spectroscopy-scientific-analysis/gamma-spectroscopy/detectors/hpge-detectors-accessories/germanium-detectors
48. Micron Semiconductor Ltd., Lancing, Sussex, England. http://www.micronsemiconductor.co.uk
49. D.X. Wang, C.J. Lin, L. Yang et al., Compact 16-channel integrated charge-sensitive preamplifier module for silicon strip detectors. Nucl. Sci. Tech. **31**, 48 (2020). https://doi.org/10.1007/s41365-020-00755-0
50. Pixie-16 User Manual, XIA LLC, https://xia.com/support/pixie-16/
51. MZ-TrigIO, XIA LLC, https://xia.com/support/mz-trigio/
52. H. Tan, W. Hennig, M. Walby *et al*., Digital data acquisition modules for instrumenting large segmented germanium detector arrays. in *2008 IEEE Nuclear Science Symposium Conference Record* (2008), pp. 3196-3200. https://doi.org/10.1109/NSSMIC. 2008.4775029
53. W. Hennig, H. Tan, M. Walby et al., Clock and trigger synchronization between several chassis of digital data acquisition modules. Nucl. Instrum. Meth. Phys. B **261**, 1000–1004 (2007). https://doi.org/10.1016/j.nimb.2007.04.181
54. S. Das, S. Samanta, R. Banik et al., A Compton suppressed detector multiplicity trigger based digital DAQ for gamma-ray spectroscopy. Nucl. Instrum. Meth. Phys. Res. A **893**, 138–145 (2018). https://doi.org/10.1016/j.nima.2018.03.035
55. H.Y. Wu, Z.H. Li, H. Tan et al., A general-purpose digital data acquisition system (GDDAQ) at Peking University. Nucl. Instrum. Meth. Phys. A **975**, 164200 (2020). https://doi.org/10.1016/j.nima.2020.164200
56. W.L. Pu, Y.L. Ye, J.L. Lou et al., Digital signal acquisition system for complex nuclear reaction experiments. Nucl. Sci. Tech. **35**, 12 (2024). https://doi.org/10.1007/s41365-024-01366-9
57. ORTEC, Model 935 quad constant-fraction 200-MHz discriminator operating and service, 2003, https://photon-science.desy.de/sites/site_photonscience/content/e62/e190204/e190208/e190212/e190216/e190217/infoboxContent190225/NIM-935_eng.pdf
58. E. Browne, J.K. Tuli, Nuclear data sheets for $A = 235$. Nucl. Data Sheets **122**, 205–292 (2014). https://doi.org/10.1016/j.nds.2014.11.002
59. L.J. Sun, M. Friedman, T. Budner et al., ^{25}Siβ^+-decay spectroscopy. Phys. Rev. C **103**, 014322 (2021). https://doi.org/10.1103/PhysRevC.103.014322
60. D.J. Vieira, R.A. Gough, J. Cerny, β-delayed proton decay of ^{29}S. Phys. Rev. C **19**, 177–187 (1979). https://doi.org/10.1103/PhysRevC.19.177
61. J.F. Ziegler, M.D. Ziegler, J.P. Biersack, SRIM-The stopping and range of ions in matter (2010). Nucl. Instrum. Meth. Phys. B **268**, 1818–1823 (2010). https://doi.org/10.1016/j.nimb.2010.02.091
62. M.J. Martin, Nuclear data sheets for $A = 152$. Nucl. Data Sheets **114**, 1497–1847 (2013). https://doi.org/10.1016/j.nds.2013.11.001
63. Yu. Khazov, A. Rodionov, F.G. Kondev, Nuclear data sheets for $A = 133$. Nucl. Data Sheets **112**, 855–1113 (2011). https://doi.org/10.1016/j.nds.2011.03.001
64. D.C. Radford, ESCL8R and LEVIT8R: Software for interactive graphical analysis of HPGe coincidence data sets. Nucl. Instrum. Meth. Phys. A **345**, 337–345 (1994). https://doi.org/10.1016/0168-9002(95)00183-2
65. M.S. Basunia, Nuclear data sheets for $A = 30$. Nucl. Data Sheets **111**, 2331–2424 (2010). https://doi.org/10.1016/j.nds.2010.09.001

Authors and Affiliations

Hao Jian[1,2] · Xin-Xing Xu[1,2,3] · Kai-Long Wang[1,2] · Jia-Jian Liu[1,2] · Chao-Yi Fu[4] · Peng-Jie Li[1] · Yan-Yun Yang[1,2] · Guang-Xin Zhang[5] · Kang Wang[1,2] · Fang-Fang Duan[1,2] · Long-Hui Ru[1,2] · Guang-Shun Li[1,2] · Bing Ding[1,2] · Yun-Hua Qiang[1,2] · Cen-Xi Yuan[5] · Jun-Bing Ma[1,2] · Shi-Wei Xu[1,2] · Yu-Feng Gao[1,2] · Rui Fan[1,2] · Fan-Chao Dai[1,2] · Si-Xian Zha[4] · Hao-Fan Zhu[1,2] · Jin-Hai Li[1,2] · Shu-Lian Qin[1,2] · Zhi-Fang Chang[1,2] · Cheng Kong[1,2] · He-Xuan Yan[1,2] · Hao-Wei Xu[1,2] · Jia-Long Ning[1,2] · Bo-Ren Liu[1,2] · Jie Zhou[1,2] · Yu-Dong Chen[1,2] · Bo-Shuai Cai[5] · Yu-Ting Wang[6] · Hong-Yi Wu[7,8] · Zhi-Xuan Wang[5] · Dong-Sheng Hou[1,4] · Hu-Shan Xu[1,2,3] · Xiao-Hong Zhou[1,2,3] · Yu-Hu Zhang[1,2,3] · Meng Wang[1,2,3] · Zheng-Guo Hu[1,2,3] · Jenny Lee[4]

✉ Xin-Xing Xu
xinxing@impcas.ac.cn

✉ Kai-Long Wang
wangkl@impcas.ac.cn

✉ Jia-Jian Liu
liujj@impcas.ac.cn

1 State Key Laboratory of Heavy Ion Science and Technology, Institute of Modern Physics, Chinese Academy of Sciences, Lanzhou 730000, China

2 School of Nuclear Science and Technology, University of Chinese Academy of Sciences, Beijing 100049, China

3 Advanced Energy Science and Technology Guangdong Laboratory, Huizhou 516003, China

4 Department of Physics, The University of Hong Kong, Hong Kong, China

5 Sino-French Institute of Nuclear Engineering and Technology, Sun Yat-sen University, Zhuhai 519082, China

6 Institute of Particle and Nuclear Physics, Henan Normal University, Xinxiang 453007, China

7 Key Laboratory of Nuclear Data, China Institute of Atomic Energy, Beijing 102413, China

8 School of Physics and State Key Laboratory of Nuclear Physics and Technology, Peking University, Beijing 100871, China